Nonlinear polarization tensor measurement with a vectorial complex field in second-harmonic-generation microscopy

Wenhui Yu ●, Xiang Li, Bing Wang, Yanping Li, Binglin Shen, Junle Qu, and Liwei Liu*

Key Laboratory of Optoelectronic Devices and Systems of Guangdong Province and Ministry of Education,
College of Physics and Optoelectronic Engineering, Shenzhen University, Shenzhen 518000, China

Polarization-sensitive second-harmonic-generation microscopy (pSHGM) allows one to determine the molecular orientation of harmonophores. Conventional point scanning based pSHGM is time consuming and subject to the assumption of the cylinder symmetry of the sample. Here, we propose a wide-field pSHGM measurement scheme that is able to measure the second-order nonlinear polarization tensor. The measurement scheme is based on first-order Born approximation, from which the relation between incident fundamental wave, second harmonic wave, and nonlinear polarization tensor has been established. It suggests that the polarization tensor can be solved by measuring the vectorial second harmonic complex fields corresponding to three independent polarization states of the incident fundamental wave. An experiment on measuring the supramolecular orientations, in terms of their symmetric axis, of myosin in rat muscle tissue has been carried out to demonstrate the proposed measurement scheme. Benefiting from the ability of recording the second harmonic signal from different positions parallelly, the proposed method possesses a higher imaging frame rate compared to point scanning based pSHGM. With the present configuration, it takes 0.01 s to acquire a 128×128 pixels image, which is mainly limited by the excitation power density for wide-field illumination. For the same data throughput using pixel-by-pixel scanning, 0.16 s acquisition time is required for a pixel dwell time of 10 μs. Having the ability of wide-field imaging and polarization measurement, the present work also lays a foundation for high-resolution SHG microscopy using computed tomography.

I. INTRODUCTION

The mechanical and rheological properties of biological tissues are closely related to the anisotropic characteristics and orientation of the forming structures [1]. Second-harmonic-generation (SHG) microscopy is a powerful technique in revealing such structures [2–4], since the SHG signal carries the information about not only intensity distribution but also polarization that is sensitive to the orientation and molecular level symmetry of the microstructure [5,6]. For instance, nanoscale research has revealed that the hyperpolarization of myosin in muscle and fibrous collagen, which are common SHG resources in biological tissue, exhibit approximate cylinder symmetry (C_∞) [7–10]. Under the cylinder symmetry assumption, the relation between SHG signal intensity and the polarization direction of an incident fundamental wave reflects the unique orientation of the harmonophores within the illumination area [11]. Existing polarization-sensitive second-harmonic-generation microscopy (pSHGM) mainly based on raster scanning of a polarization-controlled and loosely focused laser spot (in order to avoid undesired polarization variation of tight focusing), collects the SHG signal strength under different incident laser polarization directions [5,12–16]. Stoller *et al.* determined the orientation for each scanning point by continuously modulating the polarization angle of the

incident fundamental wave and measured the phase shift of the modulated SHG signal [11]. The imaging frame rate was reduced significantly compared to non-polarization-sensitive SHG microscopy by a factor determined by the points within a modulation period for resolving the phase shift with such approach. With an improved method that controlled both the polarizations of the fundamental and the SHG wave, the speed of pSHGM can be boosted to a certain extent, since fewer polarization angles were required [17–19]. However, due to the inherent low frame rate of the point scanning method, pSHGM remains limited to a small range of applications. More importantly, the above scheme based on light intensity measurement relies on the assumption that the hyperpolarization tensor is cylindrical symmetry. Even though such assumption holds for fibrous myosin and collagen in biological tissue, a more general measurement method that is not model dependent is desired for measuring more complex structures.

A promising approach to overcoming the low-speed issue would be realizing wide-field SHG imaging, in which an ensemble of sample points is illuminated and imaged simultaneously [20–25]. In these schemes, the sample was placed at the focus of a condenser lens having low numerical aperture (NA) to realize "wide-field" (relative to point scanning, usually in tens of micrometers limited by incident light power) illumination. In addition, the coherent characteristic of the harmonic signal allows one to record its complex field distribution, including both amplitude and phase distributions, via common holography methods [23]. A combination

---
*liulw@szu.edu.cn

of the intensity-based pSHGM scheme and the wide-field measurement has been realized with the speed of recording each image in milliseconds [19]. On the other hand, point scanning interferometric SHG microscopy has been proposed, which is able to resolve the polarization orientation of fibrous collagen in tendons by measuring the relative phase between a reference and the sample-induced SHG fields [16,26–28]. Although the orientation can be probed without resorting to its relationship with intensity, this technique is also limited to the cylindrically symmetric samples since there is no polarization management.

In this paper, we propose a wide-field and universal pSHGM scheme with the help of polarized complex field sensing. A model describing the relation between the vectorial SHG complex field and the second-order nonlinear polarization tensor in weakly scattering media is first derived. Under first-order Born approximation in the weakly scattering regime for both the fundamental and the second harmonic waves, we show that each harmonophore acts as an independent source emitting a spherical wave at the second harmonic (SH) of the incident wave. In this sense, the harmonophore is an analogy to the scatterer in the linear scattering process under the above weakly scattering assumption. The sample's polarization tensor can then be obtained by solving the algebra equations with different input and output polarization states. Experimentally, a microscope images the SHG field induced in the sample on a plane detector and a standard off-axis interferometer records the complex field. We further adopt complex field deconvolution, in which the complex valued amplitude point spread function (APSF) is experimentally measured, to the SHG field to improve both lateral and axial resolutions. The overall scheme is summarized as pSHGM using wide-field deconvolution of a polarized complex field (pSHGM WD PCF) technique. Finally, we demonstrate the pSHGM WD PCF for measuring the hyperpolarization tensor of myosin in rat muscle tissue.

II. THEORY

We first derive the complex and vectorial field of a generated second harmonic signal in inhomogeneous but weakly scattering nonlinear media. When the thickness of the specimen is below the transport mean free path, most of the photons are transmitted without encountering any scatter, being ballistic photons; a small portion encountered scatter once and changed their phase and transmission direction. In the wave perspective, the transmitted optical field can be decomposed into a dominating free-propagating wave and a scattered wave as perturbation [29] (Appendix B). To show this, we measured the optical field of the transmitted illumination wave (illumination wavelength $\lambda = 721$ nm) through mice (C57/Bl6) muscle tissues in different thicknesses. For a relatively thin tissue slice (20 μm), good uniform distribution both for the intensity and phase can be observed [Figs. 1(a) and 1(d)]. The standard deviation normalized to the mean value of the data along the plotted dashed lines are within 0.76% and 0.93 rad, respectively. For the 200 μm thick tissue slice, these values increase to 18.76% and >2π rad. This indicates that the nonperturbed illumination wave dominates the overall fundamental wave within thin tissues. The reduced scattering
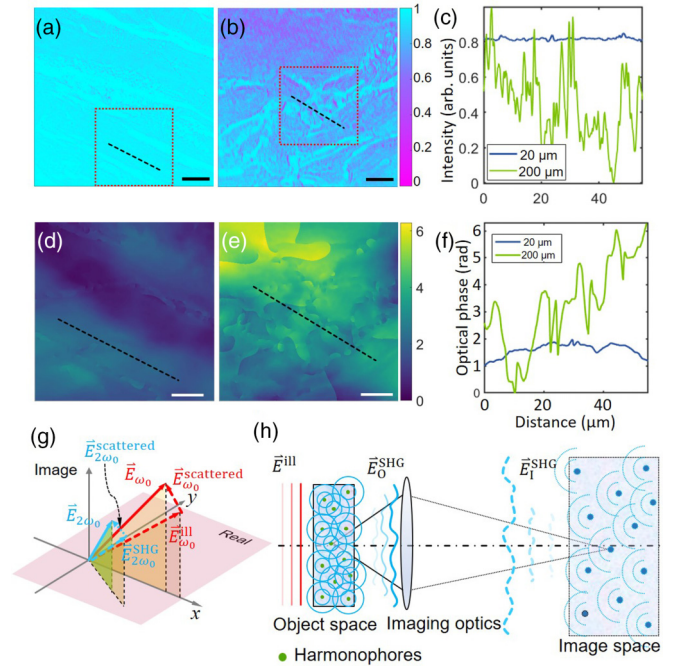

FIG. 1. Measurement results of transmitted illumination wave through tissues in different thickness and illustration of weak scattering. (a), (b) show the transmitted images for 20 and 200 μm mice (C57/Bl6) muscle tissues, respectively. (c) The intensity profiles for 20 μm tissue [dashed line in (a)] and for 200 μm tissue [dashed line in (b)]. (d), (e) show the measured phase distributions corresponding to the highlighted area in (a), (b). (f) The phase profiles for 20 μm tissue [dashed line in (d)] and for 200 μm tissue [dashed line in (e)]. (g) Schematic diagram showing the relation between overall optical field and unscattered field at the fundamental (ω_0) and the SH ($2\omega_0$) waves. Note that the polarization of the fundamental and the SH waves is shown as the projection on the *Real* plane. (h) Illustrates that the wave propagation in SHG under first-Born approximation can be viewed as the harmonophores emitting the SHG wave. The imaging optics converts the object field into a phase-conjugated field in the image space. Scale bars: (a), (b) 10 μm; (d), (e) 5 μm.

coefficient at the second harmonic wavelength (400 nm) is about 3 times larger than in the fundamental wavelength according to the survey in Ref. [30], meaning that the scattering effect of the SH wave may be of the same order as for the fundamental wave at 60 μm thickness. Therefore, considering such weak scattering, first-order Born approximation can be applied at both the fundamental and the SH waves for thin tissues (Appendix B), which suggests that the driving source for the SHG mainly includes the unscattered illumination fundamental wave and the detected SH optical field mainly comes from the unscattered SH wave.

Based on the first-order Born approximation, the governing equation of the unscattered SHG field vector $\vec{E}^{\text{SHG}}$ can be expressed as (Appendix B)

$$\nabla^2 \vec{E}^{\text{SHG}}(\vec{r}) + k_2^2 \bar{n}_2^2 \cdot \vec{E}^{\text{SHG}}(\vec{r}) \cong -k_2^2 \left[\overline{\overline{\chi}}^{(2)}(\vec{r}) : \vec{E}^{\text{ill}}_{\omega_0} \vec{E}^{\text{ill}}_{\omega_0} \right],$$

$$(1)$$

where $\overline{\overline{\chi}}^{(2)}$ is the second-order nonlinear polarization tensor and $\vec{E}_{\omega_0}^{\text{ill}}$ is the vector of the unscattered part of illuminating wave, which dominates the fundamental wave and freely propagates through the sample without perturbation; k_2 and $\bar{n}_2$ are the wave number of the SH wave in vacuum and the spatially averaged refractive index at the SH frequency, respectively (Appendix B). The vectorial Helmholtz equation (1) can be solved with the Green's function [31–33] with driving force $-k_2^2[\overline{\overline{\chi}}^{(2)}(\vec{r}) : \vec{E}_{\omega_0}^{\text{ill}}\vec{E}_{\omega_0}^{\text{ill}}]$. It simply indicates that the optical field of the SHG wave is a superposition of waves emitting by all point sources located at the harmonophores:

$$\vec{E}^{\text{SHG}}(\vec{r}) = -k_2^2 \int \overline{\overline{G}}(\vec{r}, \vec{r}')[\overline{\overline{\chi}}^{(2)}(\vec{r}') : \vec{E}_{\omega_0}^{\text{ill}}\vec{E}_{\omega_0}^{\text{ill}}]d^3\vec{r}', \quad (2)$$

where $\overline{\overline{G}}(\vec{r}, \vec{r}')$ is the Green's function. This process is illustrated in Fig. 1(h), in which an individual point within the harmonophore emits a spherical wave with the excitation of the fundamental wave and the SH field $\vec{E}^{\text{SHG}}$ is superposed by these spherical waves. With an imaging configuration, the image and the objective planes are in conjugation with a magnification factor M, so that $E_I^{\text{SHG}}(M\vec{r}) = [E_O^{\text{SHG}}(\vec{r})]^*$, in which x^* denotes the conjugation of a complex value x. Therefore, the complex value of the generated SH wave in the object space can be obtained by holographically recording the complex field in the image plane. For a linearly polarized illumination light, the generated $\vec{E}^{\text{SHG}}$ at location $\vec{r}$ within the sample can be expressed in terms of a Jones tensor according to Eq. (2) [34]:

$$\begin{bmatrix} E_x^{\text{SHG}} \\ E_y^{\text{SHG}} \end{bmatrix}_{\vec{r}} \cong \begin{bmatrix} J_{xxx} & J_{xyy} & J_{xxy} \\ J_{yxx} & J_{yyy} & J_{yxy} \end{bmatrix}_{\vec{r}} \cdot \begin{bmatrix} E_x^{\text{ill}}E_x^{\text{ill}} \\ E_y^{\text{ill}}E_y^{\text{ill}} \\ E_x^{\text{ill}}E_y^{\text{ill}} \end{bmatrix}_{\vec{r}}, \quad (3)$$

or denoted as $\vec{E}^{\text{SHG}}(\vec{r}) \cong \overline{\overline{J}}(\vec{r}) \cdot \overline{\mathbb{E}}^{\text{ill}}(\vec{r})$, where $\overline{\mathbb{E}}^{\text{ill}} = \vec{E}^{\text{ill}}\vec{E}^{\text{ill}}$ and $\overline{\overline{J}}_{ijk} = -k_2^2\overline{\overline{\chi}}_{ijk}^{(2)}$ for $j = k$ and $\overline{\overline{J}}_{ijk} = -2k_2^2\overline{\overline{\chi}}_{ijk}^{(2)}$ for $j \neq k$, according to permutation symmetry of the last two indices $\overline{\overline{\chi}}_{ijk}^{(2)} = \overline{\overline{\chi}}_{ikj}^{(2)}$. Note that if $\overline{\overline{\chi}}^{(2)}$ is anisotropic, the refractive index is very likely to be anisotropic, which means that the driving force for SHG $\vec{E}_{\omega_0^{\text{ill}}}$ may not be parallel to the incident wave. However, since the refractive index anisotropy in biological tissue is small [35], the polarization variation caused only causes an approximation error in Eq. (3). Furthermore, the components involving the z axis can be neglected compared to the other two components [36]. The error of approximation is determined by the intensity of scattering of both the fundamental and the second harmonic waves as well as the nonparallel components due to refractive anisotropy, as illustrated in Fig. 1(g). The actual relationship should be $\vec{E}_{2\omega_0}(\vec{r}) = \overline{\overline{J}}_{\text{actual}}(\vec{r}) \cdot \overline{\mathbb{E}}_{\omega_0}(\vec{r})$ instead of Eq. (3). However, since the scattering fields are weak as described above, the Eq. (3) is in fact a good approximation. To solve the 2×3 elements in $\overline{\overline{J}}^{(2)}$, three independent vectors of $\overline{\mathbb{E}}^{\text{ill}}$ can be found by selecting proper polarization of the incident beam, e.g., 0,

$\pi/4$, $\pi/2$. In this way, we have

$$\overline{\overline{E}}_{2\times3}^{\text{SHG}}(\vec{r}) = \overline{\overline{J}}_{2\times3}(\vec{r}) \cdot \overline{\overline{\mathbb{E}}}_{3\times3}^{\text{ill}}(\vec{r}), \quad (4)$$

where $\overline{\overline{E}}_{2\times3}^{\text{SHG}}$ and $\overline{\overline{\mathbb{E}}}_{3\times3}^{\text{ill}}$ are matrices formed by $\vec{E}^{\text{SHG}}$ and $\overline{\mathbb{E}}^{\text{ill}}$ with different incident polarization states. Therefore, the $\overline{\overline{\chi}}_{2\times3}^{(2)}(\vec{r})$ can be obtained by matrix inversion as

$$\overline{\overline{J}}_{2\times3}(\vec{r}) = \overline{\overline{E}}_{2\times3}^{\text{SHG}}(\vec{r}) \cdot \left[\overline{\overline{\mathbb{E}}}_{3\times3}^{\text{ill}}(\vec{r})\right]^{-1}. \quad (5)$$

Complex deconvolution. One side effect of the wide-field excitation and imaging configuration, in contrast to point scanning, is the interference between all the harmonophores, since they are excited simultaneously. Such effect in the imaging mode is embodied as the 3D complex-valued amplitude point spread function (APSF) of the imaging optics [37]. A single point SHG emitter in the sample is imaged as a spread spot, so that the image is formed by convolution between the SHG complex field and the APSF of the imaging optics:

$$\vec{E}_I(\vec{r}) = \int_{-\infty}^{+\infty} \vec{E}_O(\vec{r}')h(\vec{r} - M\vec{r}')d\vec{r}', \quad (6)$$

where $\vec{E}_I$ and $\vec{E}_O$ are the complex fields in imaging and object space, respectively; M is the magnification factor. Note that the APSF $h(\vec{r})$ is in scalar form, based on the fact that most of the imaging optics are polarization insensitive, including our experimental setup. In the spatial frequency domain, Eq. (6) can be expressed as

$$\vec{\mathcal{E}}_I(\vec{k}) = \vec{\mathcal{E}}_O(\vec{k})\hbar(\vec{k}), \quad (7)$$

where $\vec{\mathcal{E}}_I$ and $\vec{\mathcal{E}}_O$ are the spatial spectra obtained via three-dimensional (3D) Fourier transform of $\vec{E}_I$, $\vec{E}_O$; $\hbar$ is the coherent transfer function (CTF) of the imaging system. Given the ability to access the vectorial complex field of SHG by the proposed method, the complex inverse filtering technique can be applied for deconvolution of the transmitted SHG images, thus reducing the detrimental impact of interference from adjacent harmonophores. Mathematically, the inverse filtering can be performed by simple division of $\vec{\mathcal{E}}_I(\vec{k})$ by $\hbar(\vec{k})$; however, this will amplify noise for small values of $\hbar(\vec{k})$. Low-pass filtering to $\vec{\mathcal{E}}_I(\vec{k})$ is necessary to suppress noises outside the spectral region supported by the imaging optics:

$$\vec{\mathcal{E}}_I'(\vec{k}) = \vec{\mathcal{E}}_I(\vec{k})\Pi_{k\max}(\vec{k}), \quad (8)$$

where $\Pi_{k_{\max}}(\vec{k})$ is a circle-domain function that is equal to 1 within the circle domain with radius less than $k_{\max}$ and 0 otherwise, and $k_{\max}$ indicates the maximum spatial frequency that can be accepted by the imaging system ($k_{\max} = k_2\text{NA}$, where k_2 is the wave number in the second harmonic wavelength and NA is the numerical aperture). As a consequence, the CTF is accordingly bandwidth limited by dividing the low-passed spectrum $\vec{\mathcal{E}}_I'(\vec{k})$.
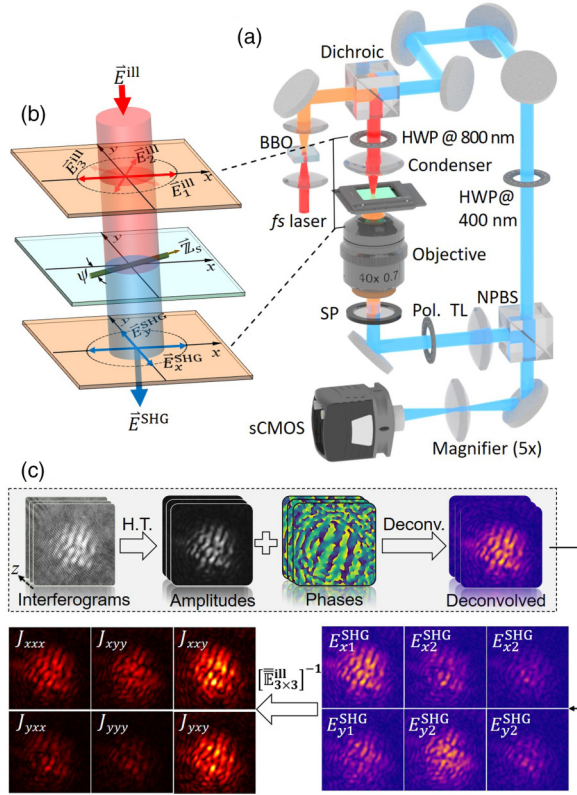
FIG. 2. Illustration of measurement scheme. (a) Experimental setup. BBO: beta barium borate crystal; HWP: half-wave plate; SP: short-pass filter; Pol.: polarizer; TL: tube lens; NPBS: nonpolarized beam splitter; sCMOS: scientific complementary metal-oxide semiconductor camera. (b) Illustration of polarization control and detection. Three linearly polarized illumination states $\vec{E}_1^{\text{ill}}$, $\vec{E}_2^{\text{ill}}$, and $\vec{E}_3^{\text{ill}}$ are used and the corresponding SH signals are detected in the x and y directions. $\vec{\mathbb{Z}}_s$ represents the symmetric axis of the sample and the included angle to the x axis is defined as the azimuthal angle ψ. (c) Signal processing flow (cf. the main text).

III. RESULTS

The proposed pSHGM WD PCF scheme was carried out on a microscope modified from our holographic SHG imaging platform [38], as shown in Fig. 2(a). A femtosecond (fs) pulse laser (Mira HP, Coherent Corp., USA) was tuned to 800 nm and focused onto a beta barium borate (BBO) crystal (Huate Material Corp., China) to generate a SHG signal as the reference in the following off-axis interferometry. The collimated fundamental and SHG waves were separated by a dichroic mirror (Chroma, T425lpxr), after which the fundamental wave was steered to the sample and the SHG signal to the reference path. The sample was placed at the focus of an aspheric condenser (ACL2018U-B, Thorlabs, USA) for wide-field illumination. The $1/e$ radius of the illumination spot was measured through the objective to be 18.86 μm [Fig. 7(b)] and the power reaching the sample was about 980 mW. This results in a peak intensity of about 6.76 GW/cm² at the sample according to the relation $I_{\text{peak}} = P_{\text{peak}}/S = [P_{\text{avg}}/(f_{\text{rep}}\tau)]/(\pi R^2)$, where the repetition rate and the pulse width were measured to be $f_{\text{rep}} = 76.3$ MHz and $\tau = 170$ fs.

Both simulation and measurement results (Fig. 7) show that the fundamental field can be well approximated as a plane wave at the condenser's focus for the thin samples that we used (less than 50 μm), which provides the exact form of the incident field [the $\overline{\overline{\mathbb{E}}}_{3\times3}^{\text{ill}}(\vec{r})$ in Eqs. (3)–(5)]. An objective (Nikon Plan Fluor 40×, NA = 0.75) collects the generated SH signal, after passing through a short-pass filter (Chroma, ET525sp-2p) and a tube lens, to a scientific complementary metal-oxide semiconductor (sCMOS) camera (Andor SONA, UK). A time-delayed configuration was set to the reference beam path for optimizing the temporal overlap between the reference and the object pulse chains. To produce a clean referencing beam, a spatial filter [not shown in Fig. 2(a)] was placed within the reference path.

Three elements were utilized to determine the excitation and the generated SH wave polarizations; i.e., a half-wave plate at the fundamental wavelength (HWP@800 nm) controlled the excitation polarization. A polarizer placed after the nonpolarized beam splitter (NPBS) determined the detected polarization and a half-wave plate at the SHG wavelength (HWP@400 nm) adapted the polarization of the reference beam to the direction of the polarizer. Figure 2(b) illustrates our polarization detection scheme. The polarization of the generated SH signal is a function of both the illuminating fundamental wave and the sample's nonlinear tensor. To resolve the tensor elements, Eq. (5) can be adopted; i.e., we illuminated the sample with three linearly polarized lasers ($\vec{E}_1^{\text{ill}}$, $\vec{E}_2^{\text{ill}}$, and $\vec{E}_3^{\text{ill}}$) sequentially and measured the complex field of the SH signal in both the x and y axes. The overall signal processing is illustrated in Fig. 2(c). For each polarization component, a stack of interferograms was recorded and deconvolved. The resulting complex field times the inverse of illumination polarization tensor allows us to obtain the sample nonlinear tensor.

The APSF was measured experimentally using a ZnO nanoparticle with a diameter of 95 nm (Nanostructured & Amorphous Materials, Inc., USA), which is able to emit a sufficient SHG signal by confining the fundamental electromagnet wave through Mie scattering [39]. With standard optics, the diffraction image of the nanoparticle at focus is only covered by a few pixels, which challenges the off-axis interferometry. Previous works used a defocused image and applied Fresnel propagation to obtain the complex field at focus. We found that the calculation of the propagation process may introduce noise due to, e.g., the uncertainty of the propagation distance and/or the retrieved complex field from the measured plane. Instead, a further 5× zoom lens (Newport M-5×, USA) was deployed for further amplification of the diffracted image of the ZnO nanoparticle so that there are sufficient fringes within the Airy disk [Fig. 3(a)]. Results were obtained with such implementation throughout the article unless specifically noted. Further amplification may reduce the effective field of view (FOV) (in our case only 20% of the origin FOV); however, since the SHG images at present are about 20 μm limited by the focus of the illumination condenser, the reduced FOV is still large enough to cover the full image. Note that even in scanning interferometric second-harmonic-generation microscopy, where the power density is sufficient high, a small effective FOV may occur due to a
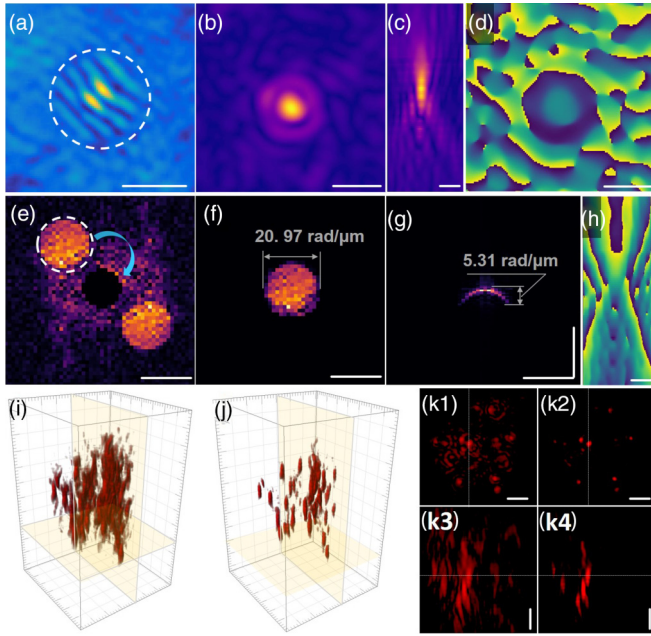
FIG. 3. Characterization of the system APSF and complex deconvolution of ZnO nanoparticle phantom. (a) Off-axis hologram of ZnO particle at focus. (b), (c) Recovered amplitudes in the xy and xz planes, respectively. (d), (h) Recovered phases in the xy and xz planes, respectively. (e) Spatial spectrum of the hologram in (a). (f) Spatial spectrum of the complex field of ZnO nanoparticle that is isolated and shifted from (e). (g) Spatial spectrum in k_x-k_z direction. (i), (j) 3D illustrations of nanoparticle suspension before and after complex deconvolution, respectively. (k1,k3) are xy and xz sections of the nanoparticle suspension highlighted in (i). (k2,k4) are xy and xz sections of the deconvolved nanoparticle suspension highlighted in (j). scale bars: (a)–(d), (h) 1 μm; (e)–(g) 20 rad/ μm; (k1–k4) 1 μm. (i), (j) 20 μm×20 μm×40 μm.
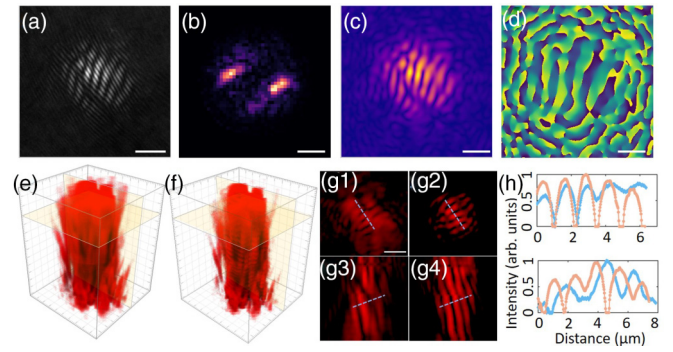

FIG. 4. Complex deconvolution results of rat muscle tissue. (a) Off-axis hologram. (b) Spatial spectrum of the complex field of the tissue that is isolated from the spatial spectrum of (a). (c), (d) Reconstructed amplitude and phase. (e), (f) 3D illustrations of the origin and complex deconvolved tissue. (g1,g3) are xy and xz sections of the muscle tissue highlighted in (e). (g2,g4) are xy and xz sections of the deconvolved muscle tissue highlighted in (f). (h) Intensity profiles along the dashed line in (g1,g2) (upper) and (g3,g4) (bottom). The blue curves correspond to the profiles of the original image, and the pink curves correspond to deconvoluted profiles. Scale bars: (a), (c), (d) and (g1–g4) 5 μm; (b) 2 rad/μm.

decrease of temporal alignment between the reference and sample SH signals at the noncentral area [16,38]. A stack of off-axis interferograms was obtained by translating the sample through focus, and each of the interferograms was processed using a Hilbert transform based technique to form a 3D APSF [Figs. 3(b)–3(d) and 3(h)]. The interferogram of the Airy disk is shown in Fig. 3(a) within the dashed circle, and upper band of its spatial spectrum [Fig. 3(e)] within the dashed circle was isolated and moved to the origin of the spatial frequency domain to complete analytic signal generation. The amplitudes at the focus in the xy and xz planes are shown in Figs. 3(b) and 3(c), in which the first minima give the resolution of 432 and 2580 nm in lateral and axial directions, respectively. They are slightly larger than theoretical predictions, due to the observable [Figs. 3(c) and 3(h)] existence of spherical aberration. On the other hand, the supported spectral range along the lateral and the axial directions was measured as 20.97 and 5.31 rad/μm, which is in good agreement with theoretical values of our objective with NA = 0.75 (lateral: $2k_{400nm} \sin(0.75) = 21.4$ rad/μm and axial: $k_{400nm}\{1 - \cos[\sin^{-1}(0.75)]\} = 5.32$ rad/μm). This shows that the CTF possesses a sharp edge at the cutoff frequency and is different from the intensity-based optical transfer function (OTF), in which the values decrease from the center to the edge [40]. Hence, the inverse filtering for the CTF deconvolution is expected to be less sensitive to noise compared with the OTF deconvolution. In addition, the 3D APSFs measured at $0°$ and $90°$ (with respect to the x axis) polarization show no significant difference, thus verifying the rationality of the scalar form of h in Eq. (6).

To test the performance of the complex deconvolution, we used a 3D uniformly distributed sample (20 μm in thickness) of ZnO nanoparticles. The interferograms were obtained by recording the off-axis holograms at different depths by translating the objective with steps of 424 nm. Figures 3(i) and 3(j) demonstrate the 3D rendering of the ZnO stack of the directly recorded and complex deconvolved results, respectively. Cross section views in the xy and xz planes demonstrate that the halo pattern was significantly reduced in both cross sections. The profile plots show that the full width at half maximum (FWHM) has improved from 545 to 420 nm and from 2407 to 1542 nm along the lateral and the axial directions, respectively (Fig. 8).

The Jones tensor of the rat muscle tissue slice was measured following the procedure illustrated in Fig. 2(c) to implement the HGM WD PCF scheme. Figure 4(a) shows one of the interferograms, in which the sarcomere bands are modulated by the interference fringes. The periods of the sarcomere were reflected by two discrete spectral peaks around the frequencies of ±4.8 rad/μm, corresponding to a period of 1.3 μm, which is in accordance with previous results [41]. The phase map of the muscle tissue [Fig. 4(d)] shows an interesting pattern where the phase changes dramatically along the direction perpendicular to the sarcomeres, while remaining relatively steady along the sarcomeres. A similar observation has been reported in the tendon fibril using point scanning based interferometric pSHG [42]. The obtained 3D complex field was deconvolved using the 3D APSF measured with the ZnO particle, and the result is shown in Figs. 4(e)–4(h).
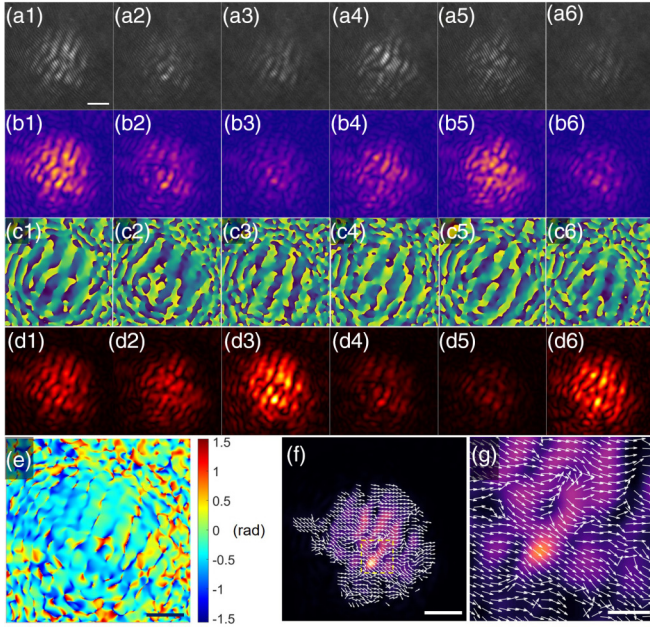
FIG. 5. Jones tensor measurement result. (a1–a6) interferograms with different polarization combinations of the fundamental (ω_0) and the SHG ($2\omega_0$) waves [p^{ω_0}, $p^{2\omega_0}$]: (a1) [$0°, 0°$]; (a2) [$0°, 90°$]; (a3) [$45°, 0°$]; (a4) [$45°, 90°$], where p stands for the linear polarization direction with respect to the x axis; (a5) [$90°, 0°$]; (a6) [$90°, 90°$]. (b1–b6) and (c1–c6) Reconstructed amplitudes and phases corresponding to the polarization combinations of the fundamental and the SHG waves the same as (a1–a6), respectively. (d1–d6) Measured Jones tensor elements for J_{xxx}, J_{xyy}, J_{xxy}, J_{yxx}, J_{yyy}, and J_{yxy}, respectively. (e) Calculated angle map of symmetrical axis orientation. (f) Measured symmetrical axis orientation of myosin. (g) Zoomed-in view within the highlighted area in (f). Scale bars: (a)–(f) 5 μm; (g) 1 μm.

The Jones tensor measurement result of the rat muscle tissue is shown in Fig. 5. Interferograms with different polarizations of both illuminating fundamental wave and the SHG wave were first captured. In the experiment, linearly polarized light with 0 °, 45 °, and 90 ° with respect to the x axis

were chosen for the illuminating polarizations. Therefore, an invertible excitation matrix in Eq. (5) was selected as

$$\overline{\overline{\mathbb{E}}}^{\text{ill}}_{3\times3}(\vec{r}) = \begin{bmatrix} 1 & 0.5 & 0 \\ 0 & 0.5 & 1 \\ 0 & 0.5 & 0 \end{bmatrix} E_0^{\text{ill}}(\vec{r}), \qquad (9)$$

where $E_0^{\text{ill}}(\vec{r})$ is the amplitude of the excitation wave, which was measured prior to the measurement (Fig. 8). Meanwhile, the SHG waves polarized in the x and y directions are measured as shown in Figs. 5(a1)–5(a6). The corresponding complex fields were retrieved from these interferograms. Having the complex fields in hand, we then performed complex deconvolution to them as shown in Figs. 5(b1)–5(b6) and 5(c1)–5(c6) for the amplitudes and phases, respectively. As can be seen, both amplitude and phase change with polarization state. A Jones matrix was obtained by applying Eq. (5) to the measured complex fields with different polarizations. The amplitudes of each Jones matrix elements are shown in Figs. 5(d1)–5(d6).

With the help of complex field measurement, we have obtained the SHG tensor elements in the laboratorial reference frame. It is more interesting, and possible if the relative orientation between the two reference frames is known, to reconstruct the unique sample-related tensor in the so-called "local frame." A general description of such operation can be found in Ref. [43]. For the accessible xy plane polarizations, only tensor elements within these two directions can be obtained. In our case, this will not induce any constraint, because under the sample preparation procedure, the fibrous myosin forming the thin muscle tissue can be well-approximated as uniaxial structure that is arranged within the image plane. During sample preparation, the muscle fibers were carefully adjusted to make sure that they are parallel to the top surface of the container. Therefore, we could calculate the axial orientation based on the Jones tensor we obtained and evaluate the rationality of the tensor to test our measurement strategy. Assume the azimuthal angle is ψ with respect to the x axis [cf. Fig. 2(b)], the Jones tensor under the laboratory frame is connected to the local frame by the following transformation equation [43]:

$$\vec{\chi}_{\textbf{Lab}} \equiv \begin{bmatrix} \chi_{xxx} \\ \chi_{xxy} \\ \chi_{xyx} \\ \chi_{xyy} \\ \chi_{yxx} \\ \chi_{yxy} \\ \chi_{yyx} \\ \chi_{yyy} \end{bmatrix}_L \cong \begin{bmatrix} 0 & 2\mathbf{s}^2c & \mathbf{s}^2c & c^3 \\ 0 & s^3 - sc^2 & -sc^2 & sc^2 \\ 0 & s^3 - sc^2 & -sc^2 & sc^2 \\ 0 & -2\mathbf{s}^2c & c^3 & sc^2 \\ 0 & -2sc^2 & s^3 & sc^2 \\ 0 & c^3 - \mathbf{s}^2c & -\mathbf{s}^2c & \mathbf{s}^2c \\ 0 & c^3 - \mathbf{s}^2c & -\mathbf{s}^2c & \mathbf{s}^2c \\ 0 & 2sc^2 & sc^2 & s^3 \end{bmatrix} \cdot \begin{bmatrix} \chi_{XYZ} \\ \chi_{YYZ} \\ \chi_{ZYY} \\ \chi_{ZZZ} \end{bmatrix}_{\textbf{LO}}, \qquad (10)$$

where the indices x, y, and z in lowercase denote the coordinate in the laboratory fframeand in uppercase denote the coordinate in the local frame, in which the symmetry axis is along the Z axis. The shorthand notations s and c represent $\sin\phi$ and $\cos\phi$, respectively. Obviously, $\chi_{xxy} = \chi_{xyx}$;

therefore, $\vec{\chi}_{\text{Lab}}$ consists of six independent elements as in Eqs. (2)–(4). The azimuthal angle ψ can be obtained as

$$\psi = \tan^{-1}\left(\frac{\chi_{yxx} + \chi_{yyy}}{\chi_{xxx} + \chi_{xyy}}\right). \qquad (11)$$
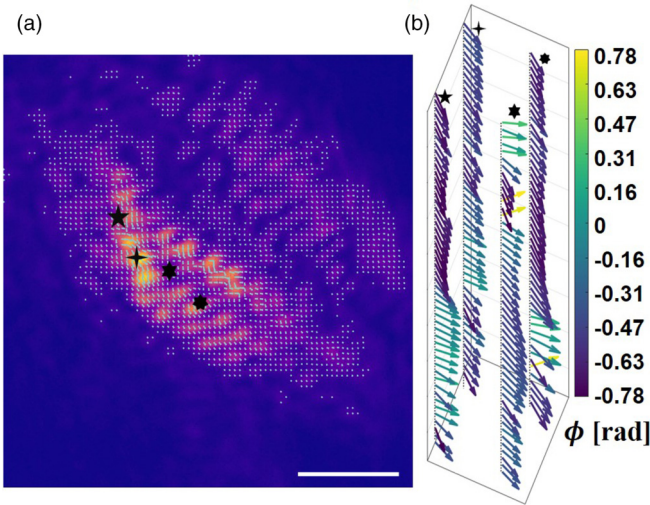
FIG. 6. Three-dimensional reconstruction result and polarization measurement of a muscle tissue section of rat (20 μm in thickness). (a) Overlay between the orientation vectors and intensity. (b) Variation of polarization direction at different depths. Each column corresponds to the locations with different markers. The color map indicates the value of the orientation angle of the symmetrical axis. Scale bars: 10 μm.

Figure 5(f) shows the obtained axis orientation and Fig. 5(g) shows the zoomed-in view within the highlighted area. The obtained molecular orientations show that the symmetrical axes are, in general, perpendicular to the direction of myosin which agrees well with a previous report [17,19]. Figure 6 shows the orientation vectors in 3D, in which the polarization variation along with the depth is shown in Fig. 6(b). To reconstruct the 3D volume image, the Jones tensor in each layer was obtained from the complex fields in different polarizations. It shows that the orientation of the symmetrical axes changes slightly, which may be due to fibril misalignment.

At the present configuration, the time for recording each image is about 0.01 s with a field of view of 20.8 μm (128×128 pixels), mainly limited by the excitation power density resulting from wide-field illumination. For the same data throughput using pixel scanning, 0.16 s is required for a pixel dwell time of 10 μs.

IV. CONCLUSION

In conclusion, we have demonstrated a pSHGM WD PCF scheme to measure a second-order nonlinear polarization tensor. We formulated the second harmonic generation in weakly scattering inhomogeneous media, under first-order Born approximation. The proposed method is based on wide-field detection, which can excite and detect all harmonophores in parallel within the imaging field of view, thus greatly improving the imaging speed. The ability of complex field detection also allows us to increase lateral and axial resolution using complex deconvolution. Using the pSHGM WD PCF measurement scheme, we presented 3D tensor reconstruction of rat mus-

cle tissue. The orientation information of the symmetric axis of the myosin molecule was obtained via the reconstructed tensor, rather than based on the cylinder symmetry assumption. Given the property of wide complex-field imaging and the similarity between SHG and linear scattering in a weakly scattering medium, we believe that this work provides important information on developing a computed tomographic method similar to optical diffraction tomography.

APPENDIX A: SAMPLE PREPARATION

A monolayer ZnO nanoparticle was prepared for measuring the systematic APSF. We dissolved 10 mg ZnO in 10 ml isopropanol, then sonicated for 10 min as the standard solution, and then diluted to 10%, 1%, and 0.1%. For each concentration of solution, we dropped 10 μl onto the glass slide and put the slide into a centrifuge machine to spread uniformly. The slides were baked at 80 °C overnight to fix the particles. The 3D ZnO stack was prepared as follows: 10 mg ZnO was dissolved in 10 ml of PDMS precursor, vibrated for 10 min as the standard solution, and then diluted to 10%, 1%, and 0.1%. They were then dispersed in PDMS and dropped on the glass for 1000 rpm spin coating. The samples were baked at 80 °C overnight for fixing.

In the research reported here, all muscle samples were from the legs of 3-month-old mice (C57/Bl6), which were euthanized, and their legs were harvested. Fifteen minutes prior to euthanasia, animals were given a 0.5 ml subcutaneous injection of 1:1000 heparin. Inhalation of 5% isoflurane was used to the animals to induce general anesthesia and 2.5% isoflurane was maintained during euthanasia. After euthanasia on mice, we took the leg muscles and immediately rinsed with PBS buffer to remove traces of hair. The harvested muscle tissue was embedded into an optimal cutting temperature compound and the orientation was carefully adjusted to make sure that the muscle fibers were parallel to the top surface of the container. This made most of the fibers within the plane perpendicular to the illumination direction during the following experiments. After freezing at −20 °C for 24 h, the sample was cut into slices with thicknesses of 5, 10, 20, and 50 μm using a frozen section machine (Leica CM3050S/Leica CM1850). The prepared slices were preserved at −80 °C before imaging experiments with our polarization dependent SHG microscope. All animal-related experiments were implemented according to the guidance of the Medical Department of Shenzhen University.

APPENDIX B: SECOND HARMONIC GENERATION AND PROPAGATION IN WEAKLY SCATTERING INHOMOGENEOUS MEDIA

We derive the electromagnetic wave propagation under first-order Born approximation within an inhomogeneous nonlinear medium in this section. The governing vectorial wave equation within medium can be expressed as

$$\nabla^2 \vec{E}(\vec{r}, t) - \frac{1}{c^2} \frac{\partial^2 \vec{E}(\vec{r}, t)}{\partial t^2} = \mu_0 \frac{\partial^2 \vec{P}(\vec{r}, t)}{\partial t^2}, \qquad \text{(B1)}$$

where $\vec{E}$ is the overall electric field and $\vec{P}$ is induced polarization. Considering second-order nonlinearity, $\vec{P}(\vec{r}, t)$ can be expanded as

$$\vec{P}(\vec{r}, t) = \varepsilon_0 \overline{\overline{\chi}}^{(1)}(\vec{r}) \cdot \vec{E}(\vec{r}, t) + \varepsilon_0 \overline{\overline{\chi}}^{(2)}(\vec{r}) : [\vec{E}(\vec{r}, t) \vec{E}(\vec{r}, t)], \tag{B2}$$

where the operator ":" denotes a third-order tensor product to the dyadic $\vec{E}(\vec{r}, t) \vec{E}(\vec{r}, t)$. Substituting Eq. (B2) in Eq. (B1) and taking the Fourier transform with respect to t, we obtain the nonlinear Helmholtz equation as

$$\nabla^2 \vec{E}(\vec{r}, \omega) + k^2(\omega) \overline{\overline{n}}^2(\vec{r}, \omega) \cdot \vec{E}(\vec{r}, \omega)$$
$$= -\frac{\omega^2}{c^2} \overline{\overline{\chi}}^{(2)}(\vec{r}) : [\vec{E}(\vec{r}, \omega) \vec{E}(\vec{r}, \omega)], \tag{B3}$$

wherein $k \frac{\omega}{c}$ is the wave number in vacuum and $\overline{\overline{n}}^2(\vec{r}, \omega) = \sqrt{1 + \overline{\overline{\chi}}^{(1)}(\vec{r}, \omega)}$ denotes the conventional refractive index (a second-order tensor in general). Under the excitation of a monochromatic wave and considering second-order nonlinear effect, the electric field within the medium can be decomposed into the fundamental and the second harmonic signals as

$$\vec{E}(\vec{r}, \omega) = A^{\omega_0}(\vec{r}) \delta(\omega - \omega_0) \hat{e}^{\omega_0} + A^{2\omega_0}(\vec{r}) \delta(\omega - 2\omega_0) \hat{e}^{2\omega_0}, \tag{B4}$$

where $A^{\omega_0}(\vec{r})$ and $A^{2\omega_0}(\vec{r})$ are the complex fields of the fundamental and the second harmonic (SH) signals, respectively; $\hat{e}^{\omega_0}$ and $\hat{e}^{2\omega_0}$ are the unit vectors of the polarizations for the fundamental and the SH signals; δ denotes the Dirac function. It should be noticed that due to anisotropy of the second-order nonlinear susceptibility tensor, the fundamental and the SH signal would not always oscillate in the same direction ($\hat{e}^{\omega_0} \nparallel \hat{e}^{2\omega_0}$). By substituting Eq. (B4) into Eq. (B3) and separating into two equations that govern the fundamental and SH, respectively, we have

$$\nabla^2 \vec{E}_{\omega_0}(\vec{r}) + k_1^2 \overline{\overline{n}}_1^2(\vec{r}) \cdot \vec{E}_{\omega_0}(\vec{r}) = 0, \tag{B5}$$

and

$$\nabla^2 \vec{E}_{2\omega_0}(\vec{r}) + k_2^2 \overline{\overline{n}}_2^2(\vec{r}) \cdot \vec{E}_{2\omega_0}(\vec{r}) = -k_2^2 [\overline{\overline{\chi}}^{(2)}(\vec{r}) : \vec{E}_{\omega_0} \vec{E}_{\omega_0}], \tag{B6}$$

where $\overline{\overline{n}}_1$ and $\overline{\overline{n}}_2$ are the spatially varying refractive indices of the fundamental and SH waves, and k_1 and k_2 are the wave

numbers of the fundamental and the SH signal in vacuum, respectively. It shows that the driving term in the right-hand side of Eq. (B6) for the second harmonic contains only the fundamental wave (including the amplitude and its polarization direction), meaning that it is the fundamental wave that generates the SH signal. In general, both the fundamental and the SH waves in Eqs. (B5) and (B6) include both the free propagating and the scattered fields, which can be written as $\vec{E}_{\omega_0} = \vec{E}_{\omega_0}^{\text{ill}} + \vec{E}_{\omega_0}^{\text{scattered}}$ and $\vec{E}_{2\omega_0} = \vec{E}^{\text{SHG}} + \vec{E}_{2\omega_0}^{\text{scattered}}$. Under first-order Born approximation, which satisfies well for weak scattering media like thin biological tissues [44], the scattered waves can be neglected compared to the unscattered wave. For the fundamental wave, we insert $\vec{E}_{\omega_0} = \vec{E}_{\omega_0}^{\text{ill}} + \vec{E}_{\omega_0}^{\text{scattered}}$ into the Eq. (B5) wave and obtain

$$\nabla^2 \vec{E}_{\omega_0}^{\text{scattered}}(\vec{r}) + k_1^2 \bar{n}_1^2 \cdot \vec{E}_{\omega_0}^{\text{scattered}}(\vec{r}) = -k_1^2 \Delta \overline{\overline{n}}_1^2(\vec{r}) \cdot \vec{E}_{\omega_0}, \tag{B7}$$

where $\Delta \overline{\overline{n}}_1^2(\vec{r}) = \overline{\overline{n}}_1^2(\vec{r}) - \bar{n}_1^2$ and $-k_1^2 \Delta \overline{\overline{n}}_1^2(\vec{r})$ is defined as the tensorial scattering potential [45], and $\bar{n}_1 = \sqrt{\overline{\overline{n}}_1^2(\vec{r}, \omega_0)_{\vec{r}}}$ is the spatially averaged refractive index at the fundamental wavelength. Note that during the derivation to Eq. (A7), the relation $\nabla^2 \vec{E}_{\omega_0}^{\text{ill}}(\vec{r}) + k_1^2 \bar{n}_1^2 \vec{E}_{\omega_0}^{\text{ill}}(\vec{r}) = 0$ has been used. The $\vec{E}_{\omega_0}$ term denotes the overall fundamental field including both the illumination and the scattered wave. Under first-order Born approximation, the $\vec{E}_{\omega_0}$ can be approximated as the unscattered part of the fundamental wave $\vec{E}_{\omega_0}^{\text{ill}}$. Therefore, the linear structure thus can be solved by conventional optical diffraction tomography [46]. With a similar approach, the governing equation for the unscattered SHG wave can be written from Eq. (B6) as

$$\nabla^2 \vec{E}^{\text{SHG}}(\vec{r}) + k_2^2 \bar{n}_2^2 \cdot \vec{E}^{\text{SHG}}(\vec{r}) \cong -k_2^2 [\overline{\overline{\chi}}^{(2)}(\vec{r}) : \vec{E}_{\omega_0}^{\text{ill}} \vec{E}_{\omega_0}^{\text{ill}}], \tag{B8}$$

where $\bar{n}_2 = \sqrt{\overline{\overline{n}}_2^2(\vec{r}, 2\omega_0)_{\vec{r}}}$ denotes the spatially averaged refractive index (second tensor in general) at the SH frequency. It is easy to find the similarity between Eqs. (B8) and (B7) and therefore solve Eq. (B8) using a similar approach. The key difference between the two equations is that Eq. (B7) can be treated as, in most cases, a scalar equation, while Eq. (B8) should consider polarization relations induced by the tensor
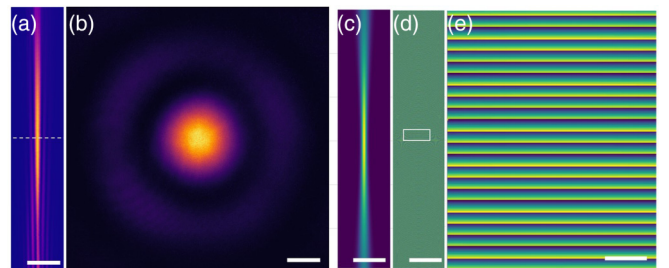

FIG. 7. Measured and simulated results of the illumination field. (a), (b) measured intensity distributions in axial and lateral planes. (c) Simulated intensity distribution in the axial plane. (d) Simulated phase map in the axial plane. Scale bar: (a)–(d) 10 μm; (e) 5 μm.
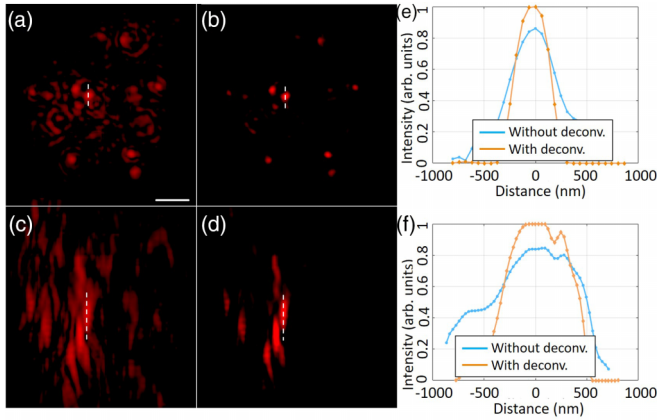
FIG. 8. Complex deconvolution result of ZnO sample. (a)–(d) are the same as Figs. 3(k1)–3(k4) in the main text. (e), (f) show the corresponding profiles along the dashed lines. Scale bars: (k1–k4) 1 μm.

calculation. Note that if $\overline{\overline{\chi}}^{(2)}$ is anisotropic, the refractive index is very likely to be anisotropic, which means that the driving force for SHG $\vec{E}_{\omega_0}^{\text{ill}}$ may not be parallel to the incident wave.

APPENDIX C: ILLUMINATION BEAM CHARACTERIZATION

The illumination beam of the microscopy system for measuring nonlinear polarization tensor is illustrated in Fig. 7, which was characterized in 3D near the focus of the condenser [cf. Fig. 2(a)].

APPENDIX D: COMPLEX DECONVOLUTION OF ZnO NANOPARTICLES

The complex deconvolution result of ZnO nano particle is illustrated in Fig. 8. The profile plots show that the full width at half maximum (FWHM) has improved from 545 to 420 nm and from 351 nm to 1542 nm along the lateral and the axial
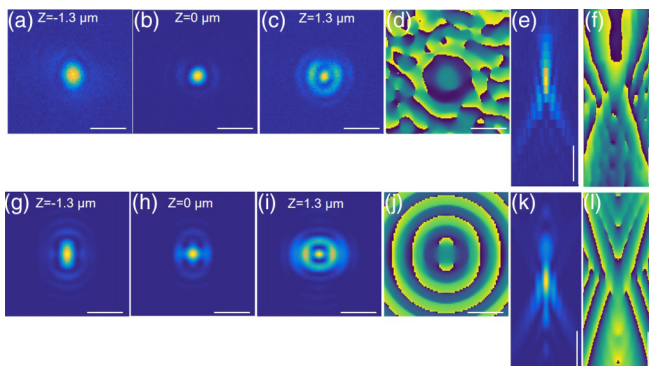

FIG. 9. Measured and simulated results of systematic APFS. (a)–(c) measured intensities of PSF at different depths. (d) Measured phase distribution at $z = 0$. (e), (f) measured intensity and phase distributions in the axial plane. (g)–(i) Simulated intensities of PSF at different depths. (j) Simulated phase distribution at $z = 0$. (k), (i) Simulated intensity and phase distributions in the axial plane. Scale bars: (a)–(d) and (g)–(j) 1 μm; (e), (f), (k), (l) 2 μm.
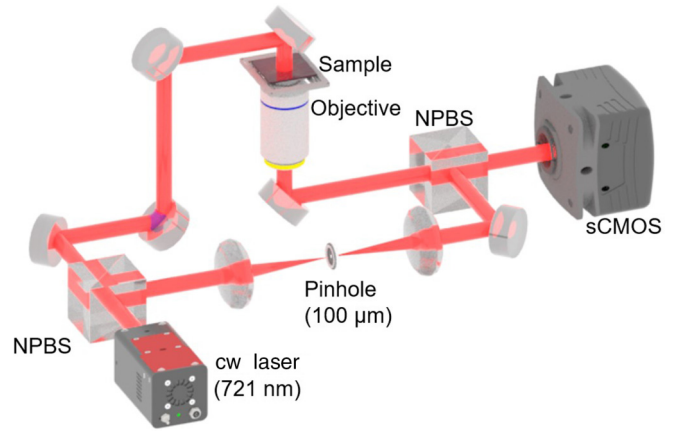

FIG. 10. Experimental setup for measuring the complex field of transmitted wave through biological tissues. NPBS: nonpolarized beam splitter. SCMOS: scientific complementary metal-oxide semiconductor camera.

directions, respectively. Figure 9 shows the measured and simulated results of systematic APFS. The consistent results between the measured and the simulated show the ability of complex field measurement of our microscopy system.

APPENDIX E: MEASURING THE OPTICAL FIELD OF TRANSMITTED LIGHT THROUGH THIN TISSUES

A typical setup of off-axis interferometry is depicted in Fig. 10. A continuous wave (cw) laser with a wavelength of 721 nm (MRL-III-650L, Changchun New Industry) was used for the imaging Mach-Zehnder interferometer. The laser was first steered to a nonpolarized beam splitter (NPBS), after which the beam was separated to perform off-axis interferometry. The sample was placed on a three-axis translation stage for wide-field illumination. An objective (Daheng Optics, GCO-213 40×, NA = 0.60) imaged the sample to a scientific complementary metal-oxide semiconductor (sCMOS) camera, which was positioned at the imaging plane of the objective where a magnified replica of the sample field was formed. The acquisition rate of the sCMOS that we used (PCO.Panda.4.2, Germany) is 48 frames/s when acquiring at the full resolution of 2048×2048 pixels. To produce a clean reference beam, a 100 μm pinhole was placed within the reference path at the common focus of a pair of lenses performing spatial filtering. Finally, the reference field was slightly tilted relative to the sample beam and interfered with the sample beam to form uniform phase modulation fringes in sCMOS. For complex field measurement of the transmitted wave, a standard algorithm of off-axis holography was adopted to reconstruct the amplitude and phase. Specifically, the camera recorded holograms and two-dimensional Fourier transform was performed to the holograms to obtain their spatial spectra. The upper band of the spectra was filtered out and was moved to the coordinate origin to remove the phase ramp of modulation. By performing inverse Fourier transform to the moved, single-banded spectra, complex fields of the sample were obtained. The background complex field was subtracted by recording the complex field without the sample.

[1] C. Verdier, Rheological properties of living materials. From cells to tissues, J. Theor. Med. **5**, 67 (2003).

[2] P. J. Campagnola and L. M. Loew, Second-harmonic imaging microscopy for visualizing biomolecular arrays in cells, tissues and organisms, Nat. Biotechnol. **21**, 1356 (2003).

[3] Y. Guo, P. P. Ho, H. Savage, D. Harris, P. Sacks, S. Schantz, F. Liu, N. Zhadin, and R. R. Alfano, Second-harmonic tomography of tissues, Opt. Lett. **22**, 1323 (1997).

[4] T. Yasui, K. Sasaki, Y. Tohno, and T. Araki, Tomographic imaging of collagen fiber orientation in human tissue using depth-resolved polarimetry of second-harmonic-generation light, Opt. Quantum Electronm **37**, 1397 (2005).

[5] S.-W. Chu, S.-Y. Chen, G.-W. Chern, T.-H. Tsai, Y.-C. Chen, B.-L. Lin, and C.-K. Sun, Studies of $\chi(2)/\chi(3)$ tensors in submicron-scaled bio-tissues by polarization harmonics optical microscopy, Biophys. J. **86**, 3914 (2004).

[6] K. R. Campbell, B. Wen, E. M. Shelton, R. Swader, B. L. Cox, K. Eliceiri, and P. J. Campagnola, 3D second harmonic generation imaging tomography by multi-view excitation, Optica **4**, 1171 (2017).

[7] J. Zhu, X. Zhang, Y. Ma, C. Zhou, and Y. Ao, Ultrastructural and morphological characteristics of human anterior cruciate ligament and hamstring tendons, Anat. Rec. Adv. Integr. Anat. Evol. Biol. **295**, 1430 (2012).

[8] D. Denning, J. I. Kilpatrick, E. Fukada, N. Zhang, S. Habelitz, A. Fertala, M. D. Gilchrist, Y. Zhang, S. A. M. Tofail, and B. J. Rodriguez, Piezoelectric tensor of collagen fibrils determined at the nanoscale, ACS Biomater. Sci. Eng. **3**, 929 (2017).

[9] D. Denning, S. Alilat, S. Habelitz, A. Fertala, and B. J. Rodriguez, Visualizing molecular polar order in tissues via electromechanical coupling, J. Struct. Biol. **180**, 409 (2012).

[10] M. Rivard, M. Laliberté, A. Bertrand-Grenier, C. Harnagea, C. P. Pfeffer, M. Vallières, Y. St-Pierre, A. Pignolet, M. A. E. Khakani, and F. Légaré, The structural origin of second harmonic generation in fascia, Biomed. Opt. Express **2**, 26 (2010).

[11] P. Stoller, K. M. Reiser, P. M. Celliers, and A. M. Rubenchik, Polarization-modulated second harmonic generation in collagen, Biophys. J. **82**, 3330 (2002).

[12] C. Yuan, Z. Wang, T. K. Borg, T. Ye, C. Baicu, A. Bradshaw, M. Zile, R. B. Runyan, Y. Shao, and B. Z. Gao, Changes in the crystallographic structures of cardiac myosin filaments detected by polarization-dependent second harmonic generation microscopy, Biomed. Opt. Express **10**, 3183 (2019).

[13] F. Radaelli, L. D'Alfonso, M. Collini, F. Mingozzi, L. Marongiu, F. Granucci, I. Zanoni, G. Chirico, and L. Sironi, μMAPPS: A novel phasor approach to second harmonic analysis for in vitro-in vivo investigation of collagen microstructure, Sci. Rep. **7**, 17468 (2017).

[14] D. Tokarz, R. Cisek, A. Golaraei, S. L. Asa, V. Barzda, and B. C. Wilson, Ultrastructural features of collagen in thyroid carcinoma tissue observed by polarization second harmonic generation microscopy, Biomed. Opt. Express **6**, 3475 (2015).

[15] S. V. Plotnikov, A. C. Millard, P. J. Campagnola, and W. A. Mohler, Characterization of the myosin-based source for second-harmonic generation from muscle sarcomeres, Biophys. J. **90**, 693 (2006).

[16] S. Bancelin, C.-A. Couture, K. Légaré, M. Pinsard, M. Rivard, C. Brown, and F. Légaré, Fast interferometric second harmonic generation microscopy, Biomed. Opt. Express **7**, 399 (2016).

[17] C. Odin, T. Guilbert, A. Alkilani, O. P. Boryskina, V. Fleury, and Y. L. Grand, Collagen and myosin characterization by orientation field second harmonic microscopy, Opt. Express **16**, 16151 (2008).

[18] C. Odin, Y. Le grand, A. Renault, L. Gailhouste, and G. Baffet, Orientation fields of nonlinear biological fibrils by second harmonic generation microscopy, J. Microscopy **229**, 32 (2007).

[19] D. G. Winters, D. R. Smith, P. Schlup, and R. A. Bartels, Measurement of orientation and susceptibility ratios using a polarization-resolved second-harmonic generation holographic microscope, Biomed. Opt. Express **3**, 2004 (2012).

[20] Y. Pu, M. Centurion, and D. Psaltis, Harmonic holography: A new holographic principle, Appl. Opt. **47**, A103 (2007).

[21] C.-L. Hsieh, Y. Pu, R. Grange, and D. Psaltis, Digital phase conjugation of second harmonic radiation emitted by nanoparticles in turbid media, Opt. Express **18**, 12283 (2010).

[22] O. Masihzadeh, P. Schlup, and R. A. Bartels, Label-free second harmonic generation holographic microscopy of biological specimens, Opt. Express **18**, 9840 (2010).

[23] E. Shaffer, C. Moratal, P. Magistretti, P. Marquet, and C. Depeursinge, Label-free second-harmonic phase imaging of biological specimen by digital holographic microscopy, Opt. Lett. **35**, 4102 (2010).

[24] E. Shaffer, N. Pavillon, J. Kühn, and C. Depeursinge, Digital holographic microscopy investigation of second harmonic generated at a glass/air interface, Opt. Lett. **34**, 2450 (2009).

[25] C.-L. Hsieh, R. Grange, Y. Pu, and D. Psaltis, Three-dimensional harmonic holographic microcopy using nanoparticles as probes for cell imaging, Opt. Express **17**, 2880 (2009).

[26] M. Rivard, K. Popov, C. Couture, M. Laliberté, A. Bertrand-Grenier, F. Martin, H. Pépin, C. P. Pfeffer, C. Brown, L. Ramunno, and F. Légaré, Imaging the noncentrosymmetric structural organization of tendon with interferometric second harmonic generation microscopy, J. Biophoton. **7**, 638 (2014).

[27] S. Yazdanfar, L. H. Laiho, and P. T. C. So, Interferometric second harmonic generation microscopy, Opt. Express **12**, 2739 (2004).

[28] J. Kaneshiro, S. Kawado, H. Yokota, Y. Uesu, and T. Fukui, Three-dimensional observations of polar domain structures using a confocal second-harmonic generation interference microscope, J. Appl. Phys. **104**, 054112 (2008).

[29] E. Wolf, Three-dimensional structure determination of semi-transparent objects from holographic data, Opt. Commun. **1**, 153 (1969).

[30] S. L. Jacques, Optical properties of biological tissues: A review, Phys. Med. Biol. **58**, R37 (2013).

[31] J.-X. Cheng and X. S. Xie, Green's function formulation for third-harmonic generation microscopy, J. Opt. Soc. Am. B **19**, 1604 (2002).

[32] D. A. Kleinman, Theory of Second Harmonic Generation of Light, Phys. Rev. **128**, 1761 (1962).

[33] R. L. Sutherland, *Nonlinear Optics*, 3rd ed., Optical Engineering (Academic Press, New York, 2008).

[34] G. J. Simpson, *Nonlinear Optical Polarization Analysis in Chemistry and Biology* (Cambridge University Press, Cambridge, 2017).

[35] P. Sun and H. Sun, Determination of the anisotropy complex refractive indices of chicken tissues *in vitro* at 650 nm, J. Eur. Opt. Soc. Rapid Publ. **5**, 10030 (2010).

[36] L. D. L. and E. M. Lifshitz, *Electrodynamics of Continuous Media*, 2nd ed. (Elsevier, Amsterdam, 1984).

[37] Y. Cotte, M. F. Toy, N. Pavillon, and C. Depeursinge, Microscopy image resolution improvement by deconvolution of complex fields, Opt. Express **18**, 19462 (2010).

[38] W. Yu, X. Li, R. Hu, J. Qu, and L. Liu, Full-field measurement of complex objects illuminated by an ultrashort pulse laser using delay-line sweeping off-axis interferometry, Opt. Lett. **46**, 2803 (2021).

[39] K. Frizyuk, I. Volkovskaya, D. Smirnova, A. Poddubny, and M. Petrov, Second-harmonic generation in Mie-resonant dielectric nanoparticles made of noncentrosymmetric materials, Phys. Rev. B **99**, 075425 (2019).

[40] J. G. McNally, T. Karpova, J. Cooper, and J. A. Conchello, Three-dimensional imaging by deconvolution microscopy, Methods **19**, 373 (1999).

[41] D. S. Gokhin, E. A. Dubuc, K. Q. Lian, L. L. Peters, and V. M. Fowler, Alterations in thin filament length during postnatal skeletal muscle development and aging in mice, Front. Physiol. **5**, 375 (2014).

[42] M. Rivard, C.-A. Couture, A. K. Miri, M. Laliberté, A. Bertrand-Grenier, L. Mongeau, and F. Légaré, Imaging the bipolarity of myosin filaments with interferometric second harmonic generation microscopy, Biomed. Opt. Express **4**, 2078 (2013).

[43] G. J. Simpson, in *Nonlinear Optical Polarization Analysis in Chemistry and Biology* (Cambridge University Press, Cambridge, 2017), pp. 475–482.

[44] C. Hu, J. J. Field, V. Kelkar, B. Chiang, K. Wernsing, K. C. Toussaint, R. A. Bartels, and G. Popescu, Harmonic optical tomography of nonlinear structures, Nat. Photon. **14**, 564 (2020).

[45] A. Saba, J. Lim, A. B. Ayoub, E. E. Antoine, and D. Psaltis, Polarization-sensitive optical diffraction tomography, Optica **8**, 402 (2021).

[46] T. Kim, R. Zhou, L. L. Goddard, and G. Popescu, Solving inverse scattering problems in biological samples by quantitative phase imaging, Laser Photon. Rev. **10**, 13 (2015).